

Lawrence Berkeley National Laboratory

Lawrence Berkeley National Laboratory

Title

Imaging CSEM data in the presence of electrical anisotropy

Permalink

<https://escholarship.org/uc/item/5r8850nk>

Author

Newman, G.A.

Publication Date

2010-06-04

Peer reviewed

IMAGING CSEM DATA IN THE PRESENCE OF ELECTRICAL ANISOTROPY

Gregory A. Newman^{*}, Michael Commer^{*} and James J. Carazzone⁺

^{*}Earth Sciences Division, Lawrence Berkeley National Laboratory, Berkeley California

⁺ExxonMobil Upstream Research Company, Houston Texas

Email: gnewman@lbl.gov

ABSTRACT

Formation anisotropy should be incorporated into the analysis of controlled source electromagnetic (CSEM) data because failure to do so can produce serious artifacts in the resulting resistivity images for certain data configurations of interest. This finding is demonstrated in model and case studies. Sensitivity to horizontal resistivity will be strongest in the broadside electric field data where detectors are offset from the tow line. Sensitivity to the vertical resistivity is strongest for over flight data where the transmitting antenna passes directly over the detecting antenna. Consequently, consistent treatment of both over flight and broadside electric field measurements requires an anisotropic modeling assumption. To produce a consistent resistivity model for such data we develop and employ a 3D CSEM imaging algorithm that treats transverse anisotropy. The algorithm is based upon non-linear conjugate gradients and full wave equation modeling. It exploits parallel computing systems to effectively treat 3D imaging problems and CSEM data volumes of industrial size. Here we use it to demonstrate the anisotropic imaging process on model and field data sets from the North Sea and offshore Brazil. We also verify that isotropic imaging of over flight data alone produces an image generally consistent with the vertical resistivity. However, superior data fits are obtained when the same over flight data are analyzed assuming an anisotropic resistivity model.

INTRODUCTION

New geophysical technologies can be combined with established seismic methods to improve the characterization of reservoir fluids in situations of practical interest. One technique that has emerged in the last several years utilizes low frequency electromagnetic (EM) energy (less than 10 Hz) to map variations in the subsurface electrical resistivity of offshore oil and gas prospects (Constable, 2006; Eidesmo et al., 2002; Ellingsrud et al., 2002, MacGregor et al., 2006). In the marine controlled source electromagnetic (CSEM) measurement technique a deep-towed electric dipole transmitter is used to excite a low-frequency electromagnetic signal that is measured on the sea floor by electric and magnetic field detectors, with the largest transmitter-detector separations exceeding ~15 km. EM data have been shown to be highly sensitive to changes in the pore fluid types and the location of oil and gas accumulations, given that oil and gas are far more resistive than brine or water. The CSEM technique therefore has the potential to extract valuable information on reservoir fluid and rock properties that may not be sensed directly by seismic methods. The technique has been used to interrogate down to reservoir depths as deep as 4 km, but benefits from structural information from seismic imaging to help delineate bulk reservoir and surrounding geologic structure (cf. MacGregor et al., 2007).

Tompkins et al. (2004) and Tompkins (2005) recognized the importance of electrical anisotropy in the interpretation of CSEM data and this result may be anticipated from measurements made in deviated wells. Horizontally layered sedimentary sequences often arise in oil and gas exploration and can exhibit transverse anisotropy on a macroscopic scale; a scale much larger than individual sedimentary layers. Transverse anisotropy is the simplest case to model (cf. Newman and Alumbaugh, 2002). Fortunately this corresponds with many situations encountered in actual geological basins where CSEM measurements are made for hydrocarbon

exploration. While it is possible to treat the more general form of the problem, where the formation anisotropy is modeled as a tensor with six independent elements (cf. Weiss and Newman, 2002), geological formations are frequently horizontally layered or nearly so and the anisotropy can be described by independent vertical and horizontal resistivities. While there are cases where anisotropy is not vertically transverse, and do not conform precisely to this scenario, vertical anisotropy still represents a significant improvement over an isotropic modeling assumption. Moreover, CSEM measurements may preclude the ability to map generalized anisotropy because of limited data coverage and acquisition geometry. Whether they can is an area of future research and is outside the scope of this paper.

Anisotropy can have a profound effect on CSEM measurements and its affect depends strongly upon acquisition geometry. The study of electrical currents in a double half-space by Lu and Xia (2007) is illuminating. Their model consists of an upper half-space that is isotropic (the sea water) and a lower half-space exhibiting transverse anisotropy (the sea bed). Vertical current flow, and hence vertical resistivity, has a much stronger impact on over flight electric field measurements (null coupled data excluded); over flight data correspond to the case where the CSEM tow line is over the detector. However, broadside measurements where the measuring antenna is offset from and parallel to the tow line are far more sensitive to horizontal currents and hence the horizontal resistivity of the sea bed.

Large-scale 3D imaging is also receiving considerable attention in the interpretation of CSEM data, (Commer et al. 2008, Commer & Newman 2008, Carazzone et al. 2008 and 2005, Gribenko and Zhdanov 2008, Plessix and Mulder 2008, Plessix and van der Sman, 2007 and 2008, Zach et al. 2008). While one-dimensional (1D) modeling and inversion is relatively easy and trial and error 3D forward modeling seemingly straight forward (Hoversten et al. 2006;

Weiss & Constable 2006, Green et al., 2005), the need for 3D imaging is necessary as the search for hydrocarbons now increasingly occurs in highly complex situations where hydrocarbon effects are subtle aspects of the total offshore geological environment. Further complicating matters is the realization that electrical anisotropy also needs to be incorporated directly into the imaging process (Newman and Commer 2008; Carazzone et al. 2008; Jing et al. 2008). Failure to properly treat anisotropy can produce misleading and sometimes un-interpretable results when broadside data is included. Merely excluding broadside data detecting antennas is frequently an issue when 3D coverage is desired.

In this paper we introduce a 3D imaging approach that treats transverse anisotropy, which appears to be relevant for many practical exploration scenarios. We employ it to study the imaging of electrical anisotropy in synthetic and field data set examples. The algorithm is based upon non-linear conjugate gradients and full wave equation modeling and is an extension of an algorithm designed for 3D isotropic media (Commer and Newman, 2008). It exploits parallel computing systems to effectively treat large-scale 3D imaging problems and CSEM data volumes of industrial size.

THE IMAGING FRAMEWORK

In setting up the 3D imaging frame work, we employ finite difference (FD) approximations to Maxwell's equations in the diffusive approximation for computing predicted data and cost functional gradients. The imaging problem is solved using a non-linear conjugate gradient scheme based upon a regularized least-squares approach implemented on parallel computing systems. Many of the details of the 3D imaging approach adopted in this paper have been published elsewhere for the isotropic case (Commer and Newman, 2008 and Newman and Boggs, 2005). Extension to treat media exhibiting transverse anisotropy is not difficult and we

provide a short discussion of the methodology here and in the appendix. For further technical details, we refer readers to the above mentioned works.

We seek to minimize the error functional

$$\phi = \frac{1}{2} \{\mathbf{D}(\mathbf{d}^p - \mathbf{d}^{\text{obs}})\}^{\mathbf{T}*} \{\mathbf{D}(\mathbf{d}^p - \mathbf{d}^{\text{obs}})\} + \frac{1}{2} \lambda_h \{\mathbf{W}\mathbf{m}_h\}^{\mathbf{T}} \{\mathbf{W}\mathbf{m}_h\} + \frac{1}{2} \lambda_v \{\mathbf{W}\mathbf{m}_v\}^{\mathbf{T}} \{\mathbf{W}\mathbf{m}_v\}. \quad (1)$$

\mathbf{T}^* denotes the transpose-conjugation operator and \mathbf{d}^{obs} and \mathbf{d}^p the observed and predicted CSEM data, consisting of n complex values of electric and magnetic fields at the detectors. A diagonal weighting matrix, \mathbf{D} , is incorporated into the error functional to help compensate for noisy measurements. Stabilization terms also appear in (1) and are designed to treat media exhibiting transverse electrical anisotropy. Parameterization of anisotropic electrical conductivity is made on a Cartesian grid, where horizontal and vertical values are assigned to m cells; note that conductivity is the reciprocal of resistivity. Solution stabilization is achieved by reducing the model curvature in three dimensions in the minimization process. To do this, we employ a FD approximation to the Laplacian (∇^2) producing a roughening matrix \mathbf{W} . \mathbf{W} acts on both the horizontal and vertical conductivity values \mathbf{m}_h and \mathbf{m}_v , which are bounded using log or hyperbolic transformations. The regularization parameters, λ_h and λ_v control the amount of smoothing admitted into the model for the two different conductivities.

In modeling transverse anisotropy an additional constraint is often imposed: $\mathbf{m}_h \geq \mathbf{m}_v$. The inequality is strictly valid for the case of thin vertical stacked layers that can be modeled as a parallel-serial circuit to electrical current flow in the horizontal and vertical directions. While it is possible to enforce this inequality in the minimization of (1) with the parameterization

$$\mathbf{m}_v = \alpha \mathbf{m}_h ; 0 \leq \alpha \leq 1, \quad (2)$$

we do not in the results reported here. Geological formations while often layered may not be sufficiently thin for (2) to hold in general. Moreover, unlike well logging problems where measurements can be designed to sense variations in thin stacked layers along a well, CSEM measurements are made on the sea bed at a remote distance from such layering. They are not capable of distinguishing thin vertical variations in layering at the same resolution that can be recognized from induction logging. Nevertheless, for the problems discussed in this paper we find equation (2) holds to a high degree even when the constraint is not explicitly enforced.

MODEL STUDY

Before presenting any field cases, model studies can yield important insight in interpreting the experimental results and serve to properly set expectations. We consider a simple model to illustrate the key features in imaging data influenced by transverse anisotropic media. Since the CSEM method is designed to map resistors we present models and imaging results that follow in the form of electrical resistivity instead of conductivity. The model shown in Figure 1 represents a simple reservoir model of 50 $\Omega\cdot\text{m}$ isotropic resistivity. Its host medium exhibits transverse anisotropy, where horizontal (ρ_h) and vertical (ρ_v) resistivities are 0.65 and 2 $\Omega\cdot\text{m}$, respectively. The sea water resistivity is isotropic (0.3 $\Omega\cdot\text{m}$) and its depth is slightly more than one kilometer. The model also exhibits a flat sea bottom, no bathymetry.

Data acquisition geometry consists of ten sail lines, spaced at 1 km (Figure 2), where the transmitter transmits at 100 meter intervals along each sail line at three frequencies, 1.25, 0.75 and 0.25 Hz. Twenty five sea bottom detectors on a uniformly sampled grid at 1 km are also shown. These detectors sample the horizontal electric fields in the orthogonal directions, E_x and E_y ; while magnetic data is also recorded with field measurements it has been our experience they

offer little more information content than what is present in the electric fields and will not be used here. Both inline data (the null coupled data arising from detector antennas perpendicular to the sail line are discarded) and broadside data are present. For computational efficiency we employ reciprocity where the detectors become computational transmitters and the transmitters the computational receivers. Numerical tests have demonstrated that the requirements of reciprocity are met to a satisfactory degree by the finite difference scheme used. Exploiting reciprocity results in 150 computational transmitters and 211,200 computational detectors.

In generating the synthetic data, we employed a much finer grid, 201^3 nodes (cell size 50 m), than used in the imaging experiments. Three different simulation grids were employed in the imaging, corresponding to 51^3 , 81^3 and 101^3 nodes and assigned to frequencies 0.25, 0.75 and 1.25 Hz. The respective cell sizes for the simulation grids are 200, 125 and 100m and are adapted to source frequency to meet the spatial sampling requirement of 4 grid nodes per skin depth. These grids are assigned to each computational transmitter depending upon frequency and are used to compute predicted data and simulate fields within the medium. The grid used to render the image is finer than the simulation grids, 120^3 , nodes. Separation of the imaging grid from the simulation grids results in significant speed up in the computations. Interested readers are referred to Commer and Newman (2008) and the appendix for more details on the grid separation approach.

Five percent Gaussian noise was added to the data and data amplitudes below an assumed noise floor of 1×10^{-13} were discarded. Data weighting was based on amplitude of each data component to insure that long offset data would make meaningful contributions in the error functional. In selecting the regularization tradeoff parameters, λ_h and λ_v , we did not enforce directionally dependent smoothing on the model. Larger tradeoff parameters produce smoother

images at the expense of an increase in the data fitting errors and smaller tradeoff parameters the opposite. Choice of the regularization parameters is dictated by the data noise and is optimally carried out using a cooling approach, where initially large tradeoff parameters are selected and then systematically reduced until the data fit to the expected noise. This can lead to multiple inversion runs at considerable cost. For purposes here, we tested several values, settling on tradeoff parameters that were fixed to a value of 0.25.

We carried out imaging of the data using two types of measurements, over flight and broadside data together and over flight data only. This choice in considering two types of data is influenced by findings that broadside data with detectors parallel to the tow line is more sensitive to horizontal resistivity, much more so than over flight data (Commer et al., 2008). Using an isotropic starting model of 1 Ω .m for the sea bed, anisotropic imaging results for both inline and broadside data are shown in the left panels of Figures 3 and 4 in cross section and in plan views. Enhanced resistivity of the reservoir zone is indicated in the vertical resistivity. Moreover, horizontal and vertical resistivities of the host medium are also captured within the sensitivity footprint of measurements. Footprints for vertical and horizontal resistivity illumination correspond to bowl like structures; outside the illumination footprint there is little to no change in the resistivity from the starting model. These structures extend to several kilometers depth over the center of the tow lines and are more clearly rendered when the horizontal and vertical resistivity are plotted as a ratio (see Figure 5). The anisotropic imaging results show that treatment of both over flight and broadside data renders sharper images than using data acquired only in the over flight mode. However, the over flight data produces a better depth estimate of the reservoir. This result arises because the imaging process was allowed to continue out to 250

iterations, compared to 100 iterations for the broadside and over flight data (see Figure 6). Improved depth resolution is observed as the problem is iterated.

Failure to image the reservoir is clear, when inline and broadside data are treated assuming isotropic media. Rapid resistivity variations down to several hundred meters below the seafloor are observed, below which a low resistivity feature, several hundred meters thick is also indicated. Resulting data misfit (the data component part in equation 1) is unacceptably large (see the top plot in Figure 6) indicating the modeling assumptions are inadequate to image the data. Inspection of the data fits shows that the cause for this poor result is due to the broadside data, specifically arising from detectors oriented parallel to the tow line. It confirms findings obtained from isotropic imaging of field data discussed below. Because inline broadside data are very sensitive to horizontal resistivity, failure to include anisotropy in the imaging process can produce disastrous image artifacts. However, the problem can be reduced by imaging only the over flight data. The result is illustrated in the right panels of Figures 3 and 4. While still inferior to anisotropic imaging enhanced resistivity is clearly associated with the reservoir. Thus over-flight data are not that sensitive to horizontal resistivity, but rather to vertical resistivity, and can be imaged using an isotropic model. Image artifacts near the sea bottom remain, though. Data misfit is also much better in this case than when both broadside and inline data are imaged assuming isotropic media (compare the corresponding top and bottom plots in Figure 6).

Results from this model study can be summarized as follows. With CSEM data, sensitivity to horizontal resistivity will be strongest in the broadside data with detectors parallel to and offset from the tow line and isotropic imaging assumptions can produce serious artifacts. While it is possible to image vertical resistivity with over flight data and still extract useful

information assuming an isotropic model, optimal results require full treatment of anisotropic media within the imaging process.

FIELD EXAMPLES

Two field examples will now be presented. It is outside of the scope of this paper to carry out a complete appraisal analysis of images produced from field data. Such an analysis requires multiple inversions using different assumptions of data noise and weighting, regularization tradeoff parameters and starting models. Tradeoffs between vertical and horizontal resistivity are certain to arise in the image process. The nature of these tradeoffs is difficult to quantify without a thorough appraisal study. Therefore our aim is more modest. It is to demonstrate that consistent anisotropic resistivity models can be produced that fit the observations better than with isotropic models and to confirm findings from the model study. When features of the resistivity models can be verified with independent information, we will do so. Encouragingly, critical features of these models can be confirmed.

Troll Field

CSEM data acquired over the Troll West Gas Province (TWGP) has been used to vet isotropic imaging algorithms developed by various researchers (cf. Commer and Newman (2008), Plessix and Mulder (2008), Li et al. (2008), among others). Here we will use the data to verify results thus far developed from the model study for anisotropic media. The gas reservoir is located offshore of Norway in the North Sea. A single 25 km long sail line crosses over the reservoir with 24 CSEM electric field detectors spaced along 12 km of the line, over the gas field. The transmitter is towed in an over flight profile mode, at an average of 25 m above the sea floor. Sea water depth varies from 300 to 360 m over the sail line. Following Commer and

Newman (2008) bathymetry effects are assumed to be minimal and ignored in the analysis. Data at two frequencies were used, 0.75 and 0.25 Hz. Simulation meshes employed for the two frequencies are based on skin depth estimations, as discussed earlier. A separate simulation mesh is assigned to each source in practice and is adapted to the source and receiver positions and their corresponding offsets. The meshing is summarized in Table 1 along with the imaging mesh. We also employed the same type of data amplitude weighting and the noise floor assumptions for the field data as was done in the model study and by Commer and Newman's (2008) earlier investigation. Vertical and horizontal regularization tradeoff parameters were fixed at 0.1 and are also based upon the tradeoff parameter that was used in the analysis of the Troll data that assumed an isotropic resistivity model. Additional details on the Troll survey logistics and the setup of the imaging experiment can be found in Johansen et al. (2005) and Commer and Newman (2008).

Figure 7 compares imaging results for anisotropic and isotropic media along with an interpreted geological section published by Johansen et al. (2005), based principally on well log and seismic data. Both isotropic and anisotropic (vertical resistivity) clearly image the gas field and correspond closely with the geological section. Even though we failed to achieve the target misfit of one (Figure 8), the anisotropic inversion produced a model that yields much data fits and a lower misfit error. Sensitivities to both horizontal and vertical resistivity variations are observed and it appears that the isotropic imaging attempts to merge these disparate resistivities into a single image. It is tempting to assign the low resistivity features to horizontal resistivity variations, but a detailed appraisal study is needed to make a determination. These features could also arise from tradeoff between vertical and horizontal resistivity parameterization as well as from stabilization/regularization employed in the imaging. Down to one kilometer depth, below

the sea bed, we observed much less variation in the vertical and horizontal resistivities than in the isotropic case; at the sea floor we observed resistivity variations for both isotropic and anisotropic cases. We believe this to be caused by detector positioning errors, as well as high sensitivity in the imaging to near sea bottom resistivity variations. Anisotropic imaging of the Troll data shows intriguing and consistent results. Even in the over flight mode, lower data fitting errors are observed compared to isotropic imaging of the data.

Campos Basin

The Campos Basin, located off-shore of Brazil is a known oil and gas province with ongoing production. In 2004, a first of a kind 3D CSEM survey was carried out to better quantify the hydrocarbon potential over part of the basin. Analysis of the Campos Basin data including the broadside measurements without taking anisotropy into account produced serious image artifacts (Commer et al., 2008). It was demonstrated that inline broadside electric field data were particularly sensitive to horizontal resistivity and could not be interpreted with an isotropic model. Carazzone et al. (2008) presented 3D anisotropy imaging results of Campos Basin data. With the treatment of anisotropy, 3D imaging of the electric field data produced interpretable results. Here we will review the findings of these works, focusing on the importance of anisotropy in the imaging process.

The Campos Basin data was acquired using ten sail lines at 5 km intervals (Figure 9), resulting in data acquisition from nearly 1 million transmitter sites using three frequencies, 1.25, 0.75 and 0.25 Hz. Twenty three detectors were deployed on the sea floor on a 40 x 40 km² grid. Horizontal grid sizes employed in the imaging mesh were kept constant at $\Delta=250$ m and vertical meshing varied from 40 to 200 m in depth. Thus the total number of nodes employed in the meshing 403 nodes along x and y , and 173 nodes vertically, and corresponds to 27.8 million

cells. Horizontal meshing for field simulation was designed upon the criteria that from each computational source midpoint, ten skin depths were spanned assuming $2 \Omega \cdot \text{m}$ resistivity for the sea bed. Grid sizes varied with frequency, $\Delta=250 \text{ m}$, 200 m and 125 m , according to frequency $f=0.125 \text{ Hz}$, 0.25 Hz and 0.5 Hz , respectively. Vertical meshing for simulation was identical to that in the image mesh to account for an accurate representation of the seafloor bathymetry. With these considerations size of the simulation meshes were reduced significantly; the number of x and y grid nodes range from 128 to 162. Solution accuracy was also verified against solutions where simulation and imaging meshes were identical.

Both over flight and broadside electric field data were imaged from this experiment using a fixed tradeoff parameters, $\lambda_h = 0.025$ and $\lambda_v = 0.025$ and $\lambda = 0.25$ for the isotropic case. A detailed 3D starting model was constructed from forward modeling of the data. In order to preserve key features of the starting model in the imaging process it was necessary to avoid setting the regularization parameters too large. Large parameters smooth out the resistivity image. We also avoided making them too small to insure for a stable image. Data weighting employed were based on the amplitude of the total electric field at each computational detector to reduce the sensitivity of weakly coupled data in the inversion process. Again reciprocity processing was used to reduce the number of computational transmitters. All three components of the electric field were included in the data analysis. Shown in Figure 10 are data fits for isotropic and anisotropic modeling assumptions along selected profiles. The isotropic results presented by Commer et al. (2008) show it is possible to fit the over flight data, as well as broadside perpendicular and vertical data as the problem is iterated, but not the broadside data arising from the detectors parallel to the tow line (inline components). A systematic fitting error is observed with broadside inline data displays, which does not dissipate as the problem is

iterated. This indicates a bias in the underlying assumptions employed in the image processing. However, with an anisotropy model both over flight and broadside inline data can be fit. These results confirm that the broadside data, particularly the inline detector components, are quite sensitive to the horizontal resistivity, and other data components to the vertical resistivity.

Commer et al. (2008) showed that the resistivity images created by the isotropic media produced strong data-acquisition overprints, particularly near the sea floor and other non-geological effects proceeding to significant depths (this resistivity image is shown in Figure 11). Subsequent modeling by Commer et al. (2008) also confirmed that improved broadside data fits (inline data) could be achieved by considering the medium that exhibits transverse anisotropy. A complete anisotropic inversion of the data was carried out by Carazzone et al. (2008). As expected, anisotropic resistivity imaging eliminated the problems observed with the isotropic resistivity assumptions. While the resistivity interpretation by Carazzone et al. (2008) did not directly reveal hydrocarbons, they demonstrated many correlations between the resistivity and seismic images which high graded the hydrocarbon potential. Shown in Figure 12, is a vertical resistivity transect across a known hydrocarbon reservoir with the seismic image superimposed. The combined image shows three interesting features. Anomaly A points to a resistivity enhancement associated with a known oil field below a seismically imaged fault. At anomaly B, the resistivity enhancement is associated with a possible trap, above a salt diapir with stratigraphic pinchouts and faulting. Lastly, anomaly C shows a possibility of conductive brine leaking up from deeper salt. While salt is considered resistive, brines originating from it can be conductive. Such brines can be buoyant and rise from depth because of dissolved gas.

CONCLUSIONS

The algorithm introduced in this paper has been designed to treat 3D resistivity media exhibiting transverse anisotropy. Within the stated modeling assumptions, this algorithm is sufficiently general and can treat large scale imaging problems and industrial size data volumes critical for 3D CSEM resistivity imaging. There are also several extensions to the algorithm worth mentioning. Joint imaging of CSEM and magnetotelluric (MT) data has much appeal as MT data acquisition comes at little additional cost and can significantly improve resolution of the resistivity image (cf. Commer and Newman, 2009). Our approach to imaging 3D transverse anisotropy is easily extended to a joint imaging framework for CSEM and MT data. In fact we have already implemented it. Extension to treat 3D media exhibiting generalized anisotropy is also possible, but will require six resistivity estimates per image cell. We doubt that all six parameters can ever be resolved given the additional number of degrees of freedom, but future research on the problem may prove otherwise. The results from the Campos Basin study are encouraging in this regard. Clearly the anisotropy present is not strictly transverse given how salt and faulting has distorted the geological bedding planes, yet a transverse anisotropic resistivity model is sufficient to fit the data and has resistivity features that are geologically consistent with well information and seismic imaging results. Perhaps the description of the resistivity with horizontal and vertical resistivity is sufficient here because the model is represented by cell values on a grid. Since the cell size is much smaller than the skin depth, the modeled anisotropy at the skin depth scale is quite general.

Case and model studies confirm the importance of electrical anisotropy in imaging CSEM data. The presence of anisotropy can be confirmed when over flight and broadside electric-field measurements are found to be inconsistent with an isotropic resistivity model.

Electric field data acquired in the broadside configuration using inline detectors are particularly sensitive to horizontal resistivity. High sensitivity to vertical resistivity is observed for over flight electric field data and broadside vertical and perpendicular data to some extent. Isotropic imaging using such data can yield meaningful results with respect to vertical resistivity (broadside measurements omitted) since there is less sensitivity to horizontal resistivity variations. Nevertheless, we find that anisotropic imaging of these data produces superior results as measured by better data fits and more consistent resistivity models.

ACKNOWLEDGMENTS

We thank PGS for permission to present the Campos Basin CSEM data and TGS-NOPEC for permission to present the seismic data. This work was carried out at Lawrence Berkeley National Laboratory, with base funding provided by the United States Department of Energy, Office of Basic Energy Sciences, under contract DE-AC02-05CH11231. Additional funding and support was provided by the ExxonMobil Corporation.

REFERENCES

Carazzone J. J., T. A. Dickens, K. E. Green, C. Jing, L. A. Wahrmond, D. E. Willen, M. Commer, and G. A. Newman, 2008, Inversion Study of a Large Marine CSEM Survey: 78th Annual International Meeting, SEG, Expanded Abstracts, 644-647.

Carazzone J. J., O. M. Burtz, K. E. Green, D. A. Pavlov, and C. Xia, 2005, Three-dimensional imaging of marine CSEM data: 75th Annual International Meeting, SEG, Expanded Abstracts, 575-578.

Commer M., G. A. Newman, J. J. Carazzone, T. A. Dickens, K. E. Green, L. A. Wahrmund, D. E. Willen, and J. Shiu, 2008, Massively parallel electrical-conductivity imaging of hydrocarbons using the IBM Blue Gene/L supercomputer: IBM Journal of Research and Development, **52**, Number ½, 93-103.

Commer M., and G. A. Newman, 2008, New advances in three-dimensional controlled-source electromagnetic inversion: Geophysical Journal International, **172**, 513-535.

Commer M., and G. A. Newman, 2009, Three-dimensional controlled-source electromagnetic and magnetotelluric joint inversion: Geophysical Journal International, **178**, 1305-1316.

Constable, S., 2006, Marine electromagnetic methods – A new tool for offshore exploration: The Leading Edge **25**, 438-444.

Eidesmo T., S. Ellingsrud, L. M. MacGregor, S. Constable, M. C. Sinha, S. Johansen, S. Kong, F. N. Westerdahl, 2002, Sea Bed Logging (SBL), a new method for remote and direct identification of hydrocarbon filled layers in deepwater areas, First Break, **20.3**, 144-152.

Ellingsrud S., T. Eidesmo, S. Johansen, M. C. Sinha , L. M. MacGregor, S. Constable, 2002, Remote sensing of hydrocarbon layers by seabed logging (SBL): Results from a cruise offshore Angola: The Leading Edge, **21**, 972-982.

Green, K. E., O. M. Burtz, L. A. Wahrmund, T. Clee, I. Gallegos, C. Xia, G. Zelewski, A. A. Martinez, M. J. Stiver, C. M. Rodriguez and J. Zhang, 2005, R3M case studies: detecting reservoir resistivity in complex settings: 75th Annual International Meeting, SEG, Expanded Abstracts, 572-574.

Gribenko A. and M. Zhdanov, 2008, Rigorous 3D inversion of marine CSEM data based on the integral equation method: *Geophysics*, **72**, WA73 – WA84.

Hoversten G. M., G. A. Newman, N. Geier, and G. Flanagan, 2006, 3D modeling of a deepwater EM exploration survey: *Geophysics*, **71**, G239-G248.

Jing, C., K. E. Green, and D. Willen, 2008, CSEM inversion: Impact of anisotropy, data coverage, and initial models: 78th Annual International Meeting, SEG, Expanded Abstracts, 604-607.

Johansen, S. E., H. E. F. Amundsen, T. Røsten, S. Ellingrud, and T. Eidesmo T., 2005, Subsurface hydrocarbons detected by electromagnetic sounding, *First Break*, **23**, 31-36.

Li, M., A. Abubakar, T. Habashy, 2008, Inversion of CSEM Data with a Model-Based Inversion Algorithm: *Geophysical Prospecting*, In Press.

Lu X. and C. Xia 2007, Understanding anisotropy in Marine CSEM data: 77th Annual International Meeting, SEG, Expanded Abstracts, 633-637.

MacGregor L., D. Andeis, T. Tomlinson, and N. Barker, 2006, Controlled-source electromagnetic imaging of the Nuggets-1 reservoir, *Leading Edge*, **25**, 984-992.

MacGregor L., N. Baker, A. Overton, S. Moody, D. Bodecott, 2007, Derisking exploration prospects using integrated seismic and electromagnetic data – a Falkland Islands case study, *Leading Edge*, **26**, 356-359.

Newman, G. A., and D. L. Alumbaugh, 2002, Three-dimensional induction logging problems, Part 2: A finite-difference solution: *Geophysics*, **67**, 484-491.

Newman, G. A., and P. T. Boggs, 2005, Solution accelerators for large-scale three-dimensional electromagnetic inverse problems: *Inverse Problems*, **20**, S151-S170.

Newman G. A., and M. Commer, 2008, The Influence of Electrical Anisotropy in 3D marine CSEM surveys: 24th Progress in Electromagnetic Research Symposium, Abstracts, 293.

R. E. Plessix and P. van der Sman, 2007, 3D CSEM modeling and inversion in complex geological settings: 77th Annual International Meeting, SEG, Expanded Abstracts, 589-593.

Plessix R-E., and W. A. Mulder, 2008, Resistivity imaging with controlled-source electromagnetic data: depth and data weighting: *Inverse Problems*, **24**, 1-22.

R. E. Plessix and P. van der Sman, 2008, Regularized and Blocky 3D controlled source electromagnetic inversion: : 24th Progress in Electromagnetic Research Symposium, Abstracts, 755-760.

Weiss C. J., and G. A. Newman, 2002, Electromagnetic induction in a fully 3-D anisotropic earth: *Geophysics*, **67**, 1104-1114.

Tompkins M., R. Weaver, L. MacGregor, 2004, Effects of vertical anisotropy on marine active source electromagnetic data and inversions: 66th Conference and Exhibition, EAGE, E026.

Tompkins M., (2005), The role of vertical anisotropy in Interpreting marine controlled-source electromagnetic data: 75th Annual International Meeting, SEG, Expanded Abstracts, 514-517.

Weiss C. J., and S. Constable, 2006, Mapping thin resistors and hydrocarbons with marine EM methods, Part II – Modeling and analysis in 3D: *Geophysics*, **71**, G321-G332.

K. S. Yee, 1966, Numerical solution of initial boundary value problems involving Maxwell's equations in isotropic media, *IEEE Trans. Ant. Prop.*, AP-14, 302–307.

J. J. Zach, A. K. Bjørke, T. Støren and F. Maaø, 2008, 3D inversion of marine CSEM data using a fast finite-difference time-domain forward code and approximate Hessian-based optimization: 78th Annual International Meeting, SEG, Expanded Abstracts, 614-618.

APPENDIX

3D CSEM INVERSE MODELING: TREATING TRANSVERSE ANISOTROPY

Minimization of (1) is carried out using a non-linear conjugate gradient scheme, with a line search to control the model step. Typically only three to four solutions of the forward modeling problem for each transmitter and excitation frequency are necessary to obtain the model update. This iterative scheme is ideal for large scale data sets and imaging volumes that typically arise for CSEM type problems. Solution for isotropic media has been developed by Commer and Newman (2008) and Newman and Boggs (2005). Here we will discuss modifications to the above mentioned approach for media exhibiting transverse anisotropy.

Large computational demands arise in solving realistic 3D CSEM field simulation problems. In solving such problems we employ finite-difference approximations over a simulation mesh because of their simplicity and accuracy. Now the simulation mesh, Ω_s , is not required to be identical to the mesh, Ω_m , employed for the inverse modeling. Hence, significant computational efficiencies can be realized when the meshes are different for large-scale problems (cf. Commer and Newman, 2008). Solution of the forward problem is obtained through a sparse linear system of equations,

$$\mathbf{K}\mathbf{E}=\mathbf{S}. \tag{A1}$$

It is solved using iterative Krylov methods (cf. Newman and Boggs, 2005). \mathbf{K} is a sparse complex symmetric matrix with 13 non-zero entries per row. \mathbf{E} is the electric field sampled on the mesh using a staggered grid (Yee, 1966) and \mathbf{S} is the field sourcing term, with Dirichlet boundary conditions imposed in (A1).

This matrix equation is a discrete representation of the operator

$$\nabla \times \nabla \times E^s + i\omega \mu_o \underline{\sigma} E^s = -i\omega \mu_o (\underline{\sigma} - \underline{\sigma}^b) E^b, \quad (\text{A2})$$

where

$$\underline{\sigma} = \begin{pmatrix} \sigma_h & 0 & 0 \\ 0 & \sigma_h & 0 \\ 0 & 0 & \sigma_v \end{pmatrix} \quad \text{and} \quad \underline{\sigma}^b = \begin{pmatrix} \sigma_h^b & 0 & 0 \\ 0 & \sigma_h^b & 0 \\ 0 & 0 & \sigma_v^b \end{pmatrix}. \quad (\text{A3})$$

Equation (A2) is a 3D vector equation for the scattered electric field arising in conductive media exhibiting transverse anisotropy. It assumes a time harmonic dependence of $e^{i\omega t}$, where ω represents angular frequency and $i = \sqrt{-1}$. The electrical conductivity, $\underline{\sigma}$, is described by a tensor, where σ_h and σ_v denote the conductivities in the horizontal and vertical directions; magnetic permeability, μ_o , is assumed to be that of free space. We prefer a scattered field solution to the field equations over a total field, because of accuracy issues, particularly in the vicinity of the transmitter. In a scattered-field formulation we are also required to specify a background electric field, E^b . Thus the total electric field is given by $E = E^b + E^s$. Here we have selected a background field arising from 1D layered media that also exhibits transverse anisotropy, $\underline{\sigma}^b$. The background field can be easily and quickly computed from Hankel transforms. Once the electric field is determined from equation (A1), the magnetic field follows from Faraday's law by numerically approximating the curl of the electric field at the various nodal points and interpolating these fields to the points of interests. In a scattered field formulation, background fields will need to be added to the interpolated fields to yield the total fields.

Following Commer and Newman (2008), the inversion unknowns \mathbf{m}_h and \mathbf{m}_v belong to Ω_m , and a mapping is required from Ω_s to Ω_m in computing the gradient of equation (1). This gradient is used for updating the conductivity model in the inversion process using the non-linear conjugate gradient scheme previously mentioned. Consider the data component of the gradient, $\nabla\varphi_d(\mathbf{m}_h, \mathbf{m}_v)$, which involves only the first term in equation (1),

$$\nabla\varphi_d(\mathbf{m}_h, \mathbf{m}_v) = -Re\{(\mathbf{D}\mathbf{J}^T) \mathbf{D}(\mathbf{d}^p - \mathbf{d}^{obs})^*\} \quad (\text{A4})$$

The above expression requires the Jacobian matrix, which we split into horizontal and vertical components based on horizontal and vertical conductivity sensitivities:

$$\mathbf{J} = \begin{Bmatrix} \mathbf{j}^h \\ \mathbf{j}^v \end{Bmatrix}. \quad (\text{A5})$$

Here specific elements are given by

$$j_{jk}^h = \frac{\partial d_j^p}{\partial m_{h_k}} \quad \text{and} \quad j_{jk}^v = \frac{\partial d_j^p}{\partial m_{v_k}} \quad j=1, \dots, N ; k=1, \dots, M , \quad (\text{A6})$$

with N and M representing the number of data points and inverse modeling cells. In terms of the electric field on the simulation mesh, Ω_s , the Jacobian elements can also be expressed by

$$J_{jk}^h = \mathbf{q}_j^T \frac{\partial \mathbf{E}}{\partial m_{h_k}} \quad (\text{A7})$$

and

$$J_{jk}^v = \mathbf{q}_j^T \frac{\partial \mathbf{E}}{\partial m_{v_k}}, \quad (\text{A8})$$

where \mathbf{q}_j is a column vector for the j th data point that maps the electric field solution on Ω_s to the detector location. Next differentiating (A1) with respect to m_{h_k} and m_{v_k} we have

$$\frac{\partial \mathbf{E}}{\partial m_{h_k}} = \mathbf{K}^{-1} \left(\frac{\partial \mathbf{S}}{\partial m_{h_k}} - \frac{\partial \mathbf{K}}{\partial m_{h_k}} \mathbf{E} \right) \quad (\text{A9})$$

and

$$\frac{\partial \mathbf{E}}{\partial m_{v_k}} = \mathbf{K}^{-1} \left(\frac{\partial \mathbf{S}}{\partial m_{v_k}} - \frac{\partial \mathbf{K}}{\partial m_{v_k}} \mathbf{E} \right). \quad (\text{A10})$$

Using the chain rule we can express equations (A9 and A10) in terms of the conductivities on the simulation mesh, where

$$\frac{\partial \mathbf{E}}{\partial m_{h_k}} = \mathbf{K}^{-1} \left(\sum_{l=1}^{P(k)} \frac{\partial \mathbf{S}}{\partial \sigma_{h_l}} \frac{\partial \sigma_{h_l}}{\partial m_{h_k}} - \sum_{l=1}^{P(k)} \frac{\partial \mathbf{K}}{\partial \sigma_{h_l}} \frac{\partial \sigma_{h_l}}{\partial m_{h_k}} \mathbf{E} \right) \quad (\text{A11})$$

and

$$\frac{\partial \mathbf{E}}{\partial m_{v_k}} = \mathbf{K}^{-1} \left(\sum_{l=1}^{Q(k)} \frac{\partial \mathbf{S}}{\partial \sigma_{v_l}} \frac{\partial \sigma_{v_l}}{\partial m_{v_k}} - \sum_{l=1}^{Q(k)} \frac{\partial \mathbf{K}}{\partial \sigma_{v_l}} \frac{\partial \sigma_{v_l}}{\partial m_{v_k}} \mathbf{E} \right) \quad (\text{A12})$$

The summations are over conductivity cells on the simulation mesh that overlap cell k on the modeling mesh (Figure 13). For the k_{th} model (inversion) cell, we have $P(k)$ and $Q(k)$ horizontal and vertical conductivities overlapping from the simulation mesh. For the isotropic case, Commer and Newman (2008) provides an explicit formula for $\frac{\partial \sigma_l}{\partial m_k}$ based upon a material averaging scheme of Moskow et. al. (1999). Extension to media exhibiting transverse anisotropy is straight forward, with material averaging for horizontal and vertical conductivities each done separately. Computational efficient forms for the gradient (the data part) follow by substituting equations (A11 and A12) into equations (A7 and A8), followed by substitution into equation (A4). Note we never explicitly form \mathbf{K}^{-1} or the Jacobian when evaluating the gradient. For

computational efficiency an adjoint state method is exploited. We refer the reader to Newman and Boggs (2005) for further details.

TABLES

Grid	Number of cells	Δx	Δy	Δz	
Ω_m	$125 \times 41 \times 59$	250	250	100	
		$\Delta_x^{min} / \Delta_x^{max}$	$\Delta_y^{min} / \Delta_y^{max}$	$\Delta_z^{min} / \Delta_z^{max}$	$f(Hz)$
Ω_s^1	$85 \times 41 \times 85$	125/250	250/250	25/200	0.25 (<i>f</i> 1)
Ω_s^2	$110 \times 43 \times 85$	75/125	125/250	25/200	0.75 (<i>f</i> 2)

Table 1. List of model and simulation grids for the Troll data inversion. Ω_m and Ω_s^1 and Ω_s^2 correspond to the modeling mesh and the two simulations meshes designed for frequencies 0.25 and 0.75 Hz. Grid sizes are in meters.

FIGURE CAPTIONS

Figure 1. Shown is a simple 3D model to illustrate the key features in imaging data influenced by transverse anisotropy.

Figure 2. The data acquisition geometry consists of ten sail lines, spaced at 1 km. Twenty five sea bottom detectors are shown and the projection of the reservoir is indicated by the dashed square. Different measurement configurations are also illustrated.

Figure 3. Images cross sections of the test model assuming isotropic and anisotropic media directly over the reservoir, $y=0$ km. The left column consider both over flight and broadside data. Those on the right are images based only on over flight data.

Figure 4. Illustrated are images depth sections at 1 km of the test model data assuming isotropic and anisotropic media. The left column consider both over flight and broadside data. Those on the right are images based only on over flight data.

Figure 5. Cross-sectional ratio plots of horizontal (ρ_h) to vertical (ρ_v) resistivity of the test model, directly over the reservoir, $y=0$ km. Plots are based upon inline and inline plus broadside data illustrated on a log scale. They were generated from the anisotropic imaging results of Figure 3. A value 0.33 corresponds to the correct ratio for the background. Ratios near one indicate there is little change from the starting model, and consequently the recovered model has little to no sensitivity to the data at these image points.

Figure 6. Convergence plots for isotropic and anisotropic media. The top plots shows the data misfits plotted against inversion iteration for broadside and over flight data. Ideally, the target misfit is one assuming that noise in the data is Gaussian. The lower plot is only for over flight data. Note also that number of iterations used for anisotropic imaging differs in the two plots.

Figure 7. Imaging results for the Troll field. The top part of the figure is the interpretation published by Johansen et al. (2005) based on well log and seismic data. The middle and lower panels shows the isotropic and anisotropic CSEM imaging results.

Figure 8. Convergence plots for isotropic and anisotropic media for the Troll data set.

Figure 9. Shown are the layout of the sail lines and twenty three sea bottom detectors, indicated by the plus symbols, for the Campos Basin CSEM survey. The bathymetry is in meters below sea level with a contour interval of 50 m. Data acquired at the embolden detector, shown closest to the upper right hand corner of the plot, is used to illustrate the data fitting errors for broadside and over flight data in Figure 10 along sail lines RC06 and RC07.

Figure 10. Plotted are data fits to over flight data (line RC07) (left, (a) isotropic and (c) anisotropic) and broadside inline data (line RC06) (right, (b) isotropic and (d) anisotropic). Data acquired at the emboldened detector and the plots are projected along the x axis (see Figure 9). The observed data are plotted in black, the predicted data at iteration 72 in green, and the predicted data for the starting model in red. Data correspond to a frequency of 0.125 Hz. The anisotropic starting model uses a vertical resistivity identical to that used in the isotropic imaging. However, the horizontal resistivity was set to one third the vertical resistivity below the water bottom.

Figure 11. Shown is the average resistivity computed over three depth ranges assuming an isotropic medium. The figure is from Commer et al. (2008) and shows (a) average resistivity from the water bottom to 500m depth, (b) depth interval 500 to 1500 m and (c) 2,500 to 2,500 m. Resistivity is rendered on a base 10 log scale.

Figure 12. Rendered at the top is the average vertical resistivity map from 500 to 2500 m below the seafloor, superimposed with sail lines used to acquire the Campos Basin data. Also shown are lease block boundaries outlined in violet and known hydrocarbon deposits (black contours). The cross-section at the bottom shows the vertical resistivity image along the indicated transect. The EM image is shown together with seismic reflection horizons. Results presented by Carazzone et al. (2008).

Figure 13. Concept of separate model/inversion and simulation grids is illustrated in two dimensions. The dashed grid corresponds to the model/inversion mesh Ω_m and the solid grid to the simulation mesh Ω_s . Field simulation on a staggered grid requires that the electrical conductivity be sampled at the edges of the simulation grid; illustrated here is the case for σ_h .

The zone outlined in red corresponds to the averaging area on the modeling grid from which σ_h is to be computed on the simulation grid using Moskow et al. 1999, aggregation formula, shown at the top of the figure.

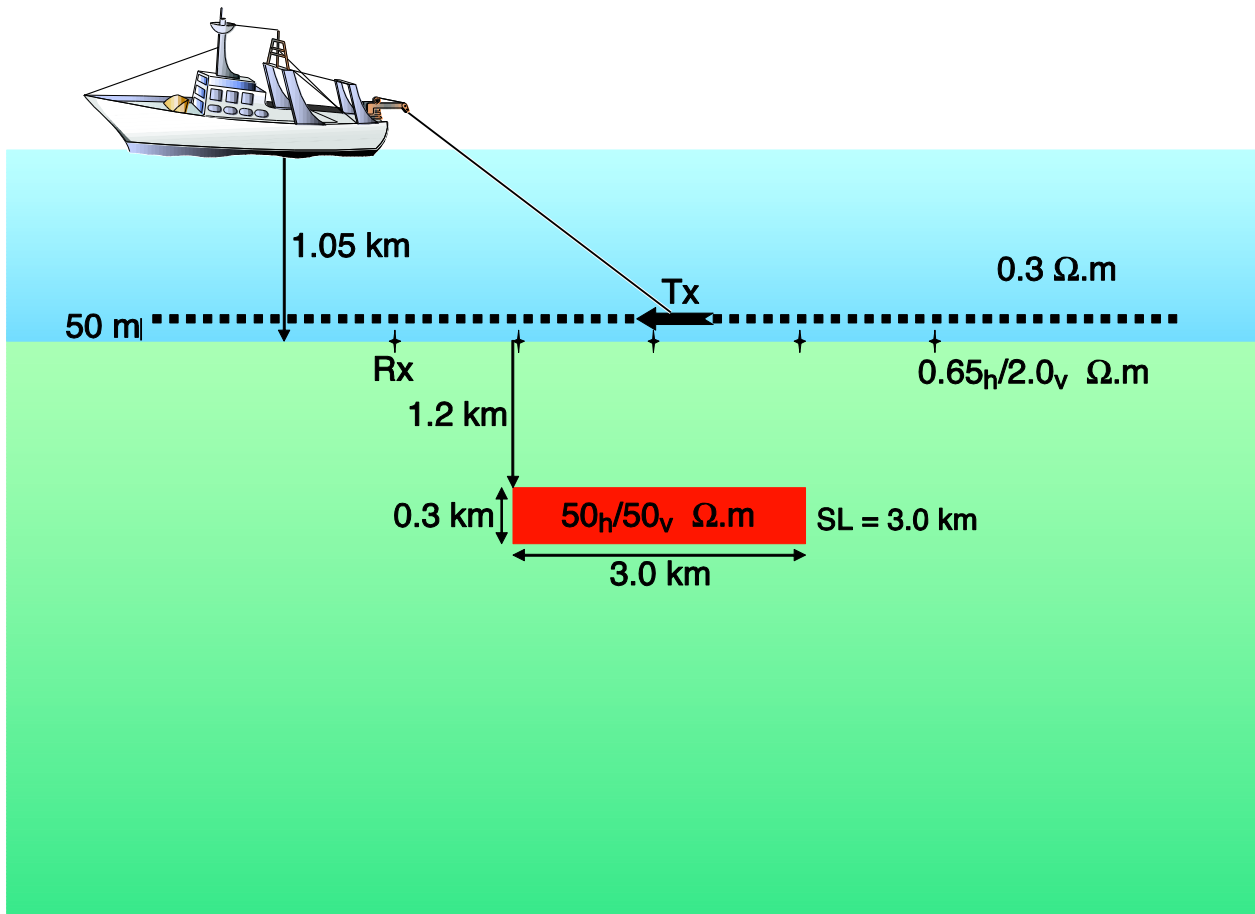


Figure 1.

Measurement Configurations

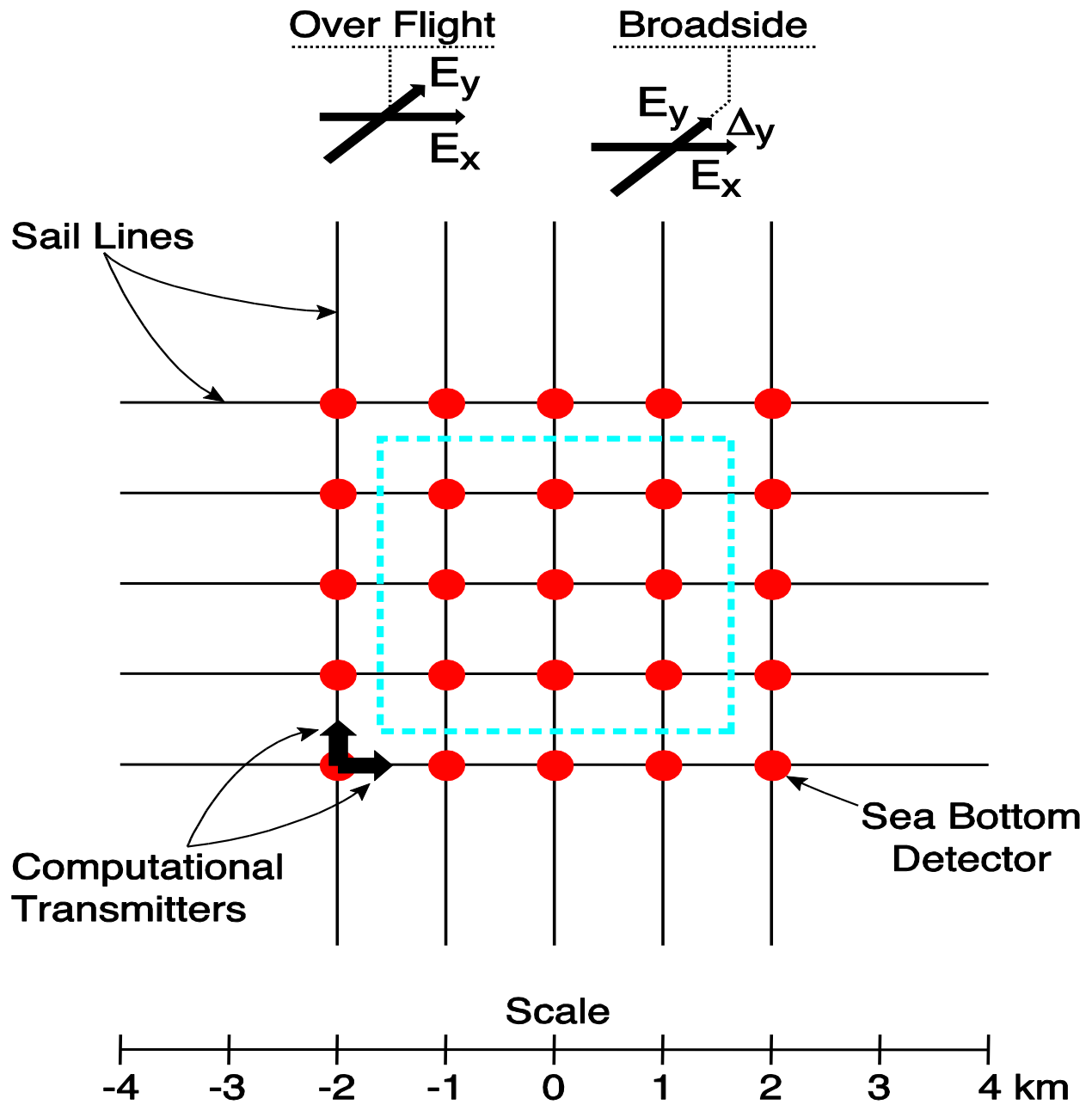


Figure 2.

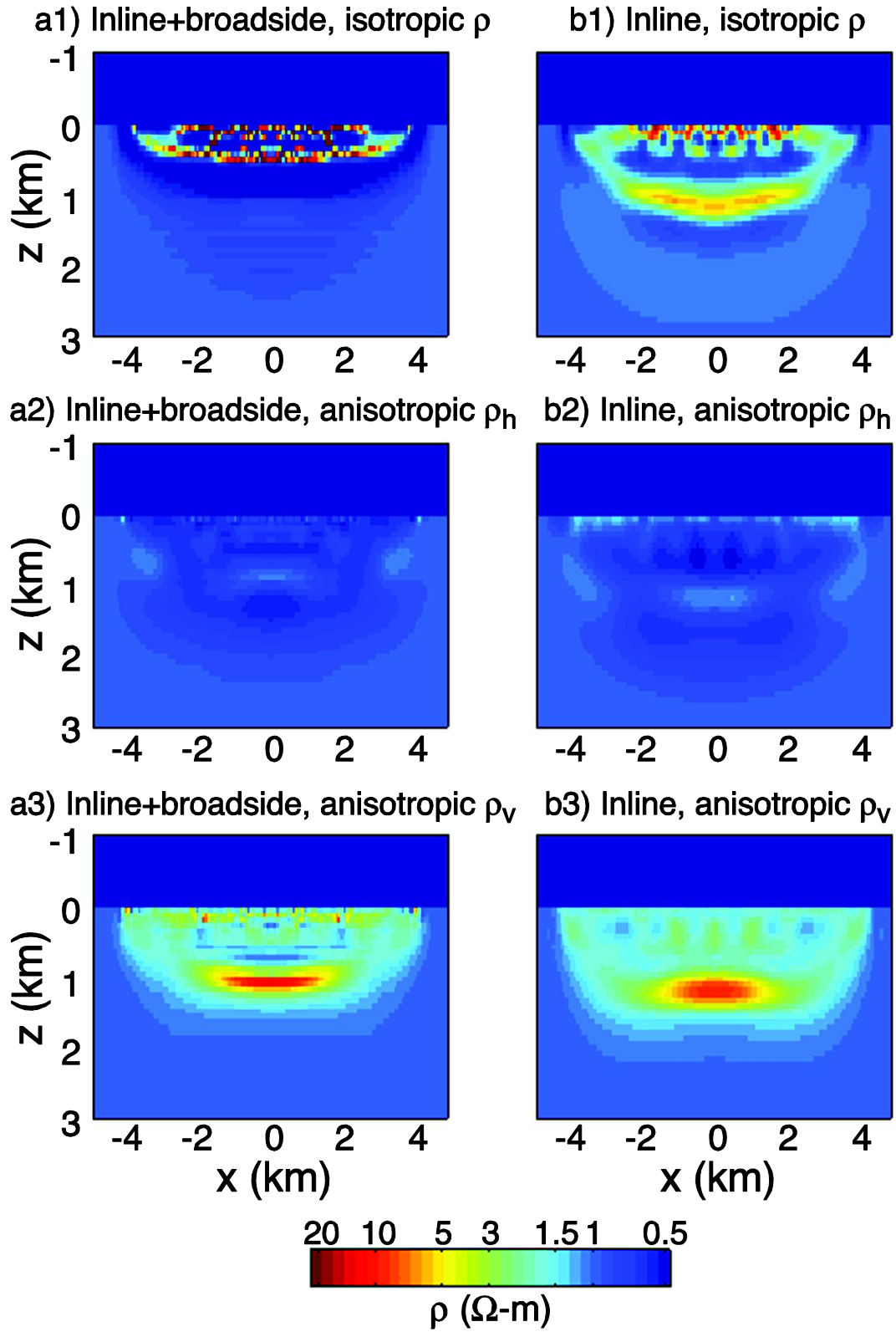


Figure 3.

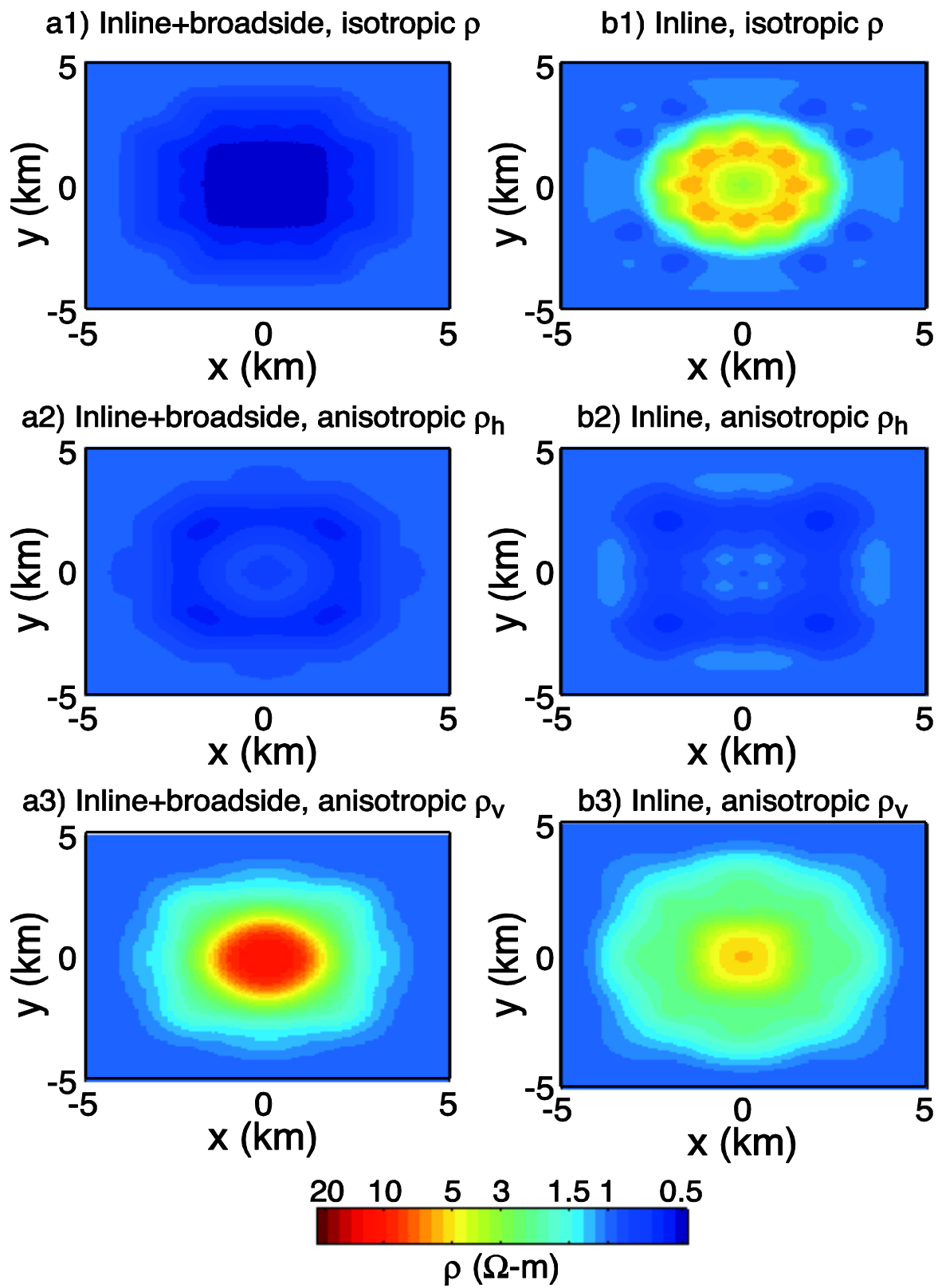


Figure 4.

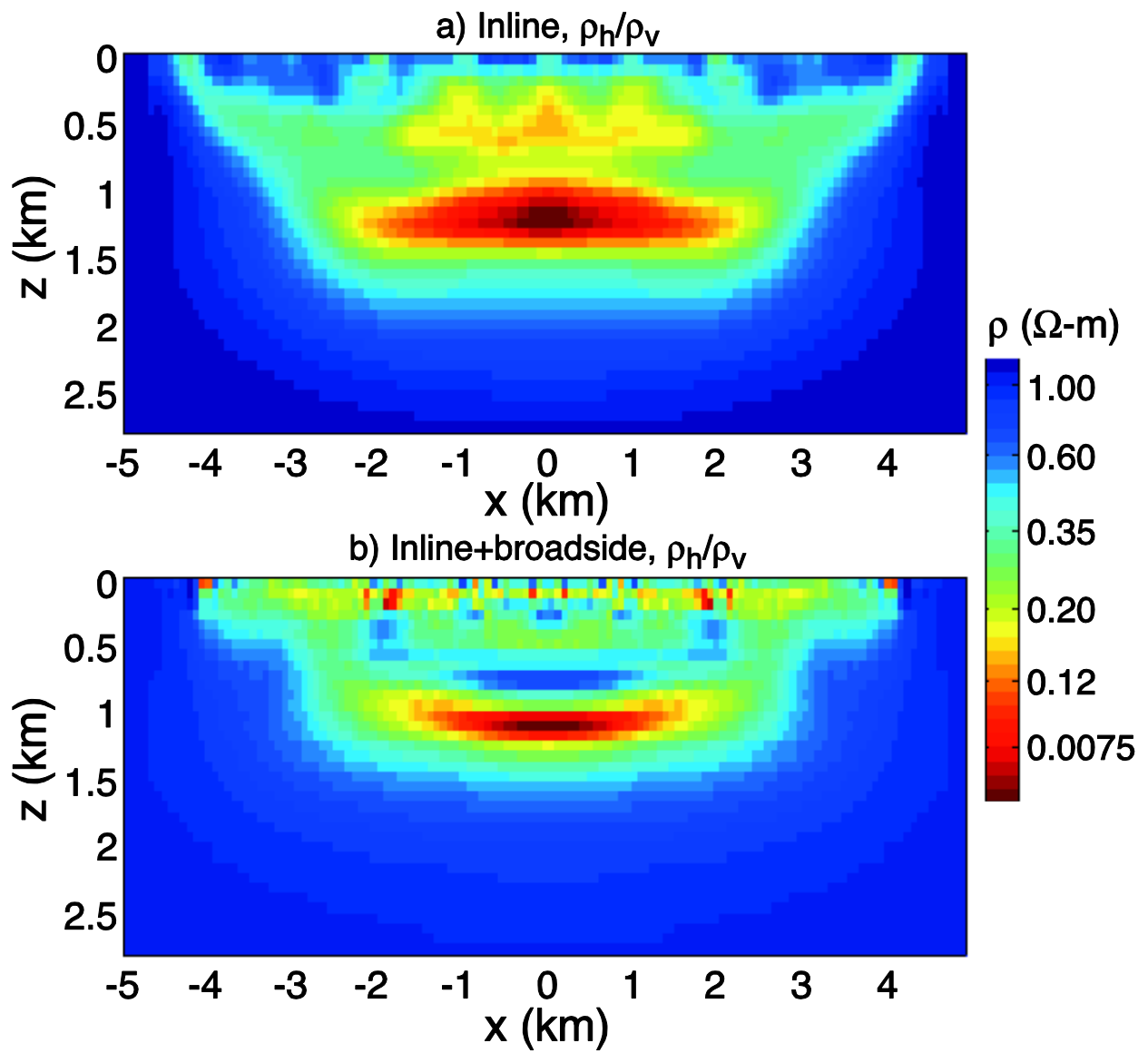


Figure 5.

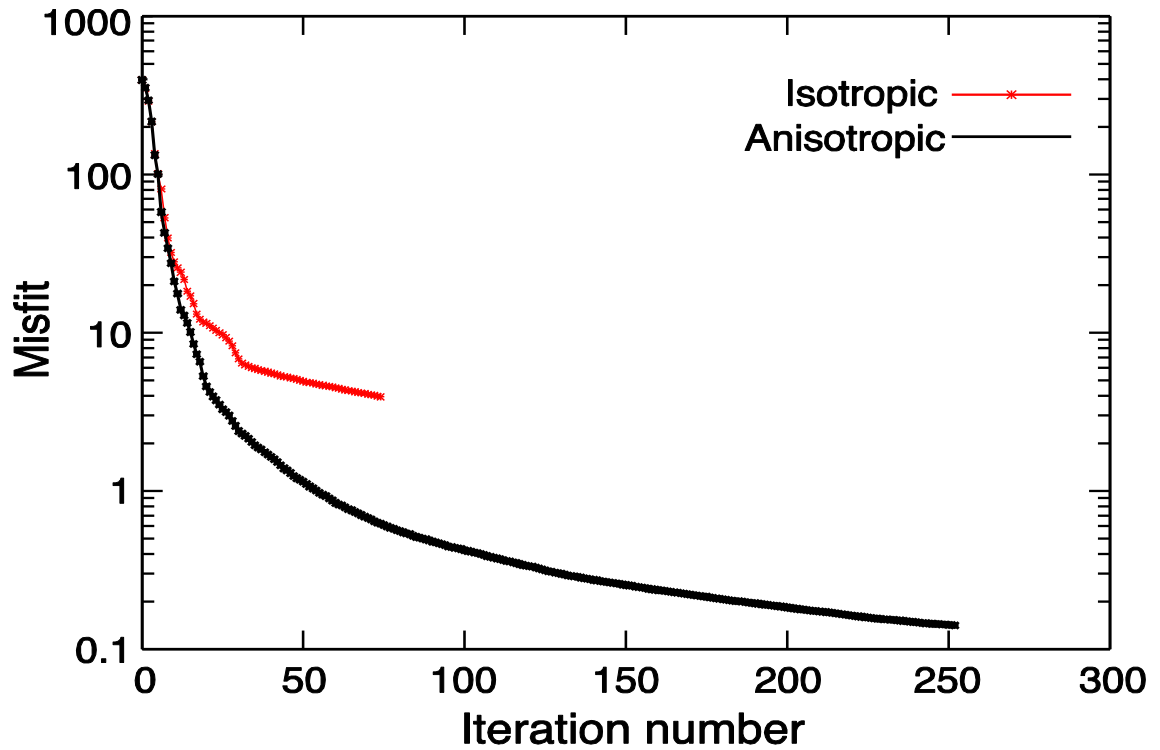
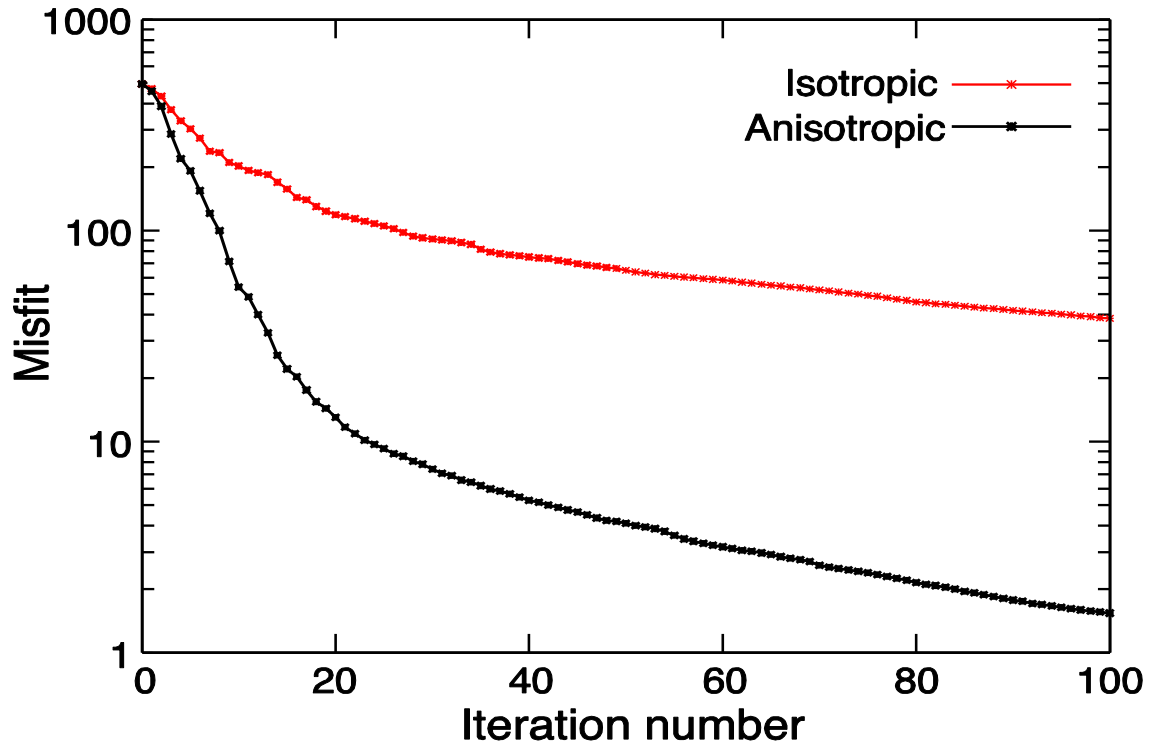


Figure 6.

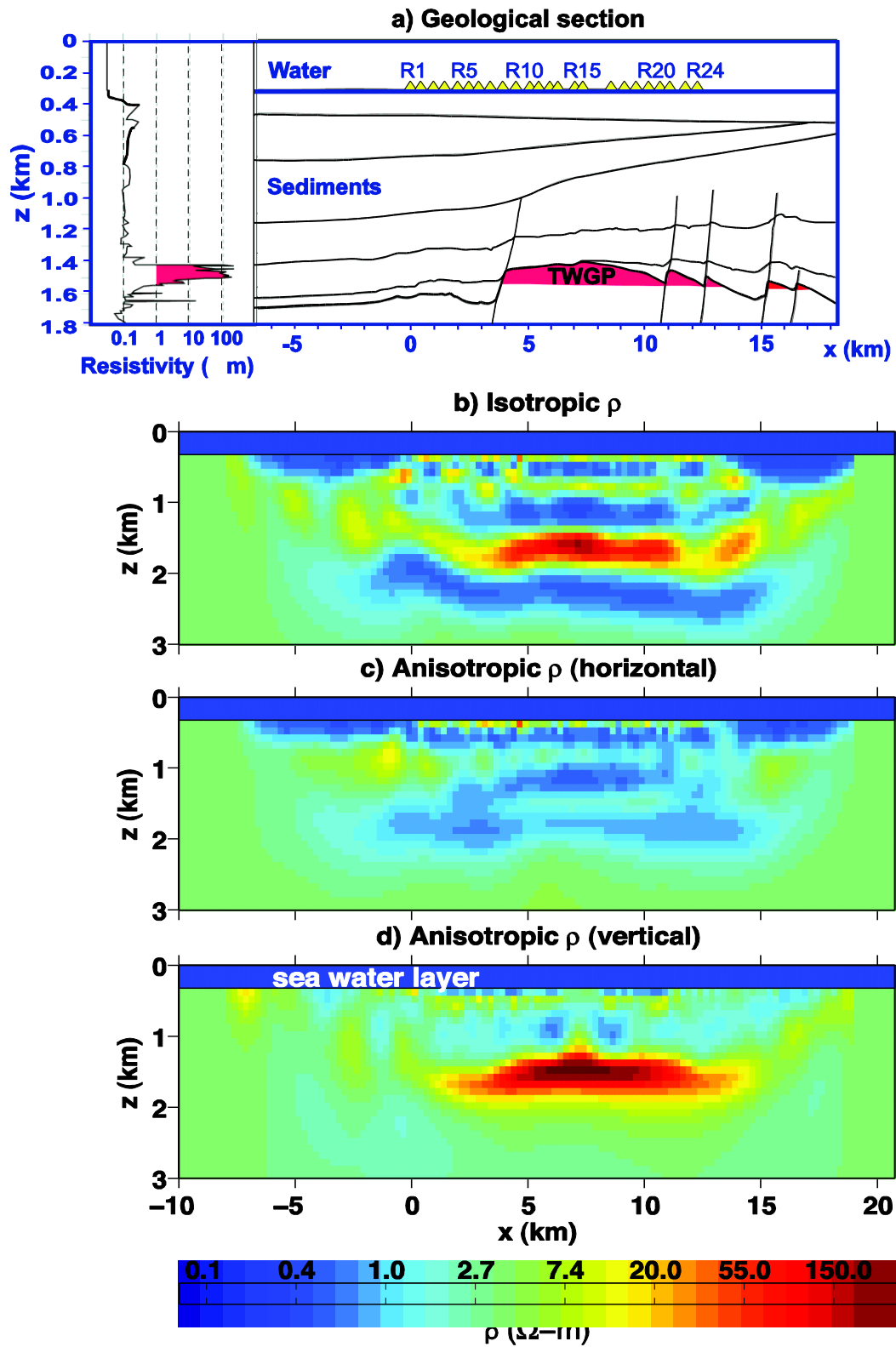


Figure 7.

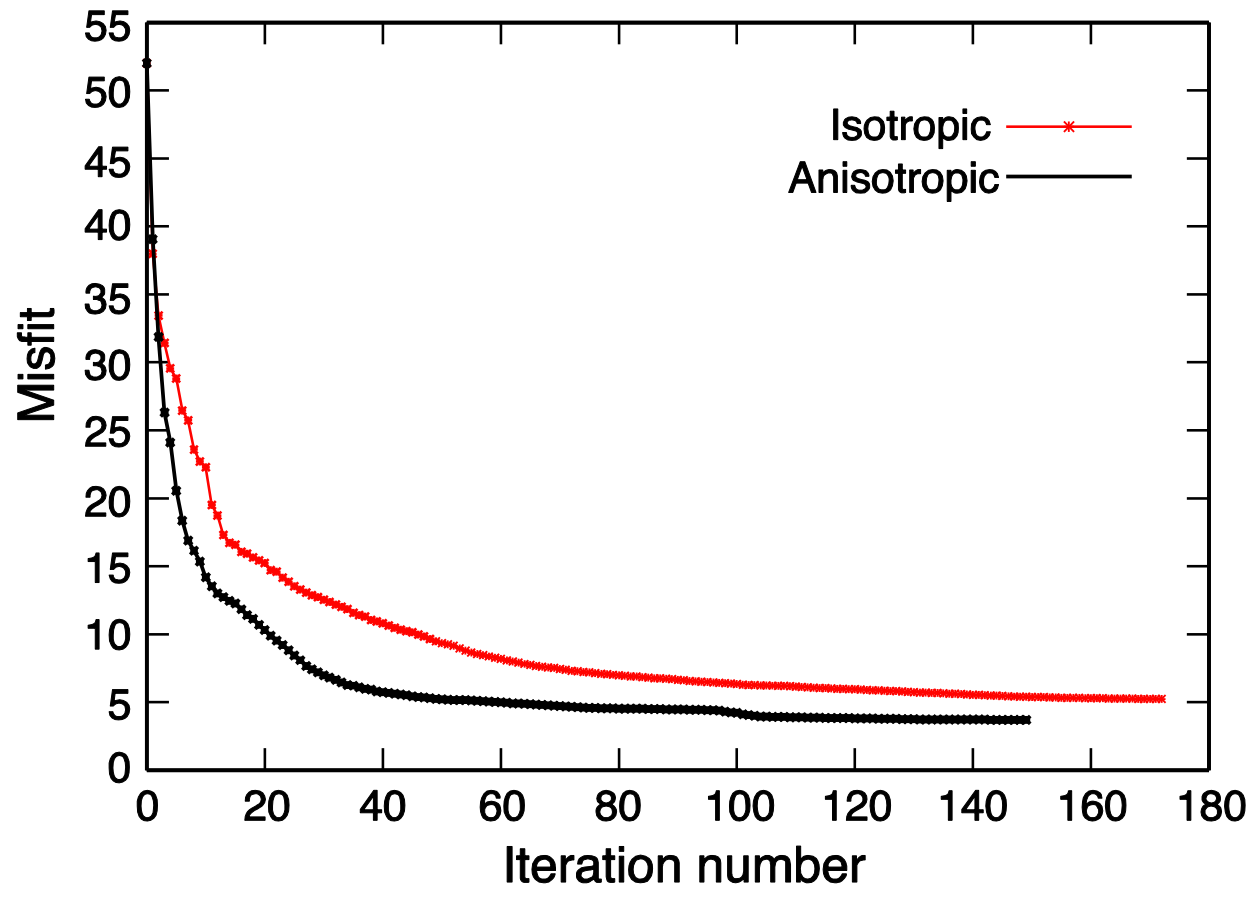


Figure 8.

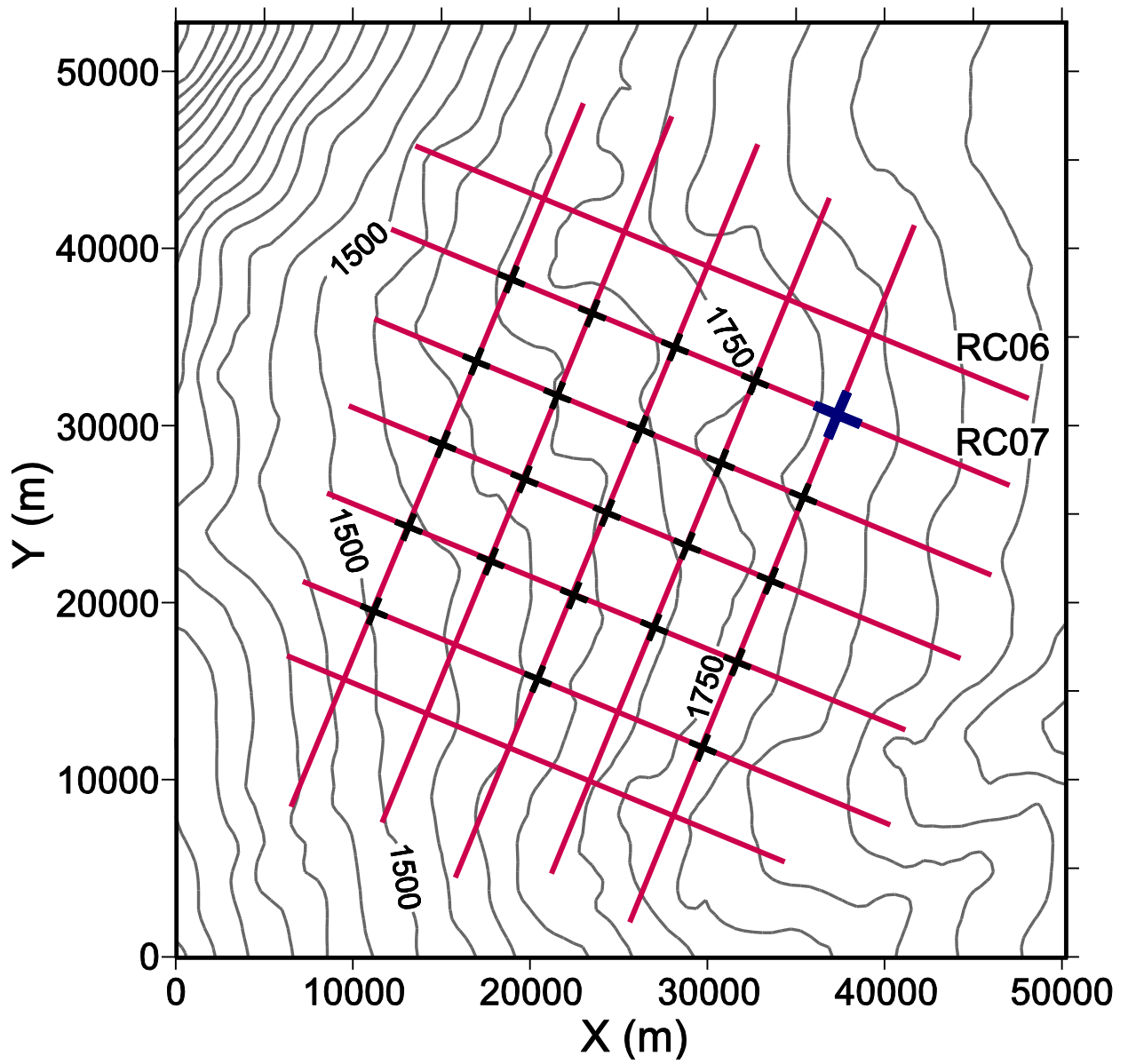


Figure 9.

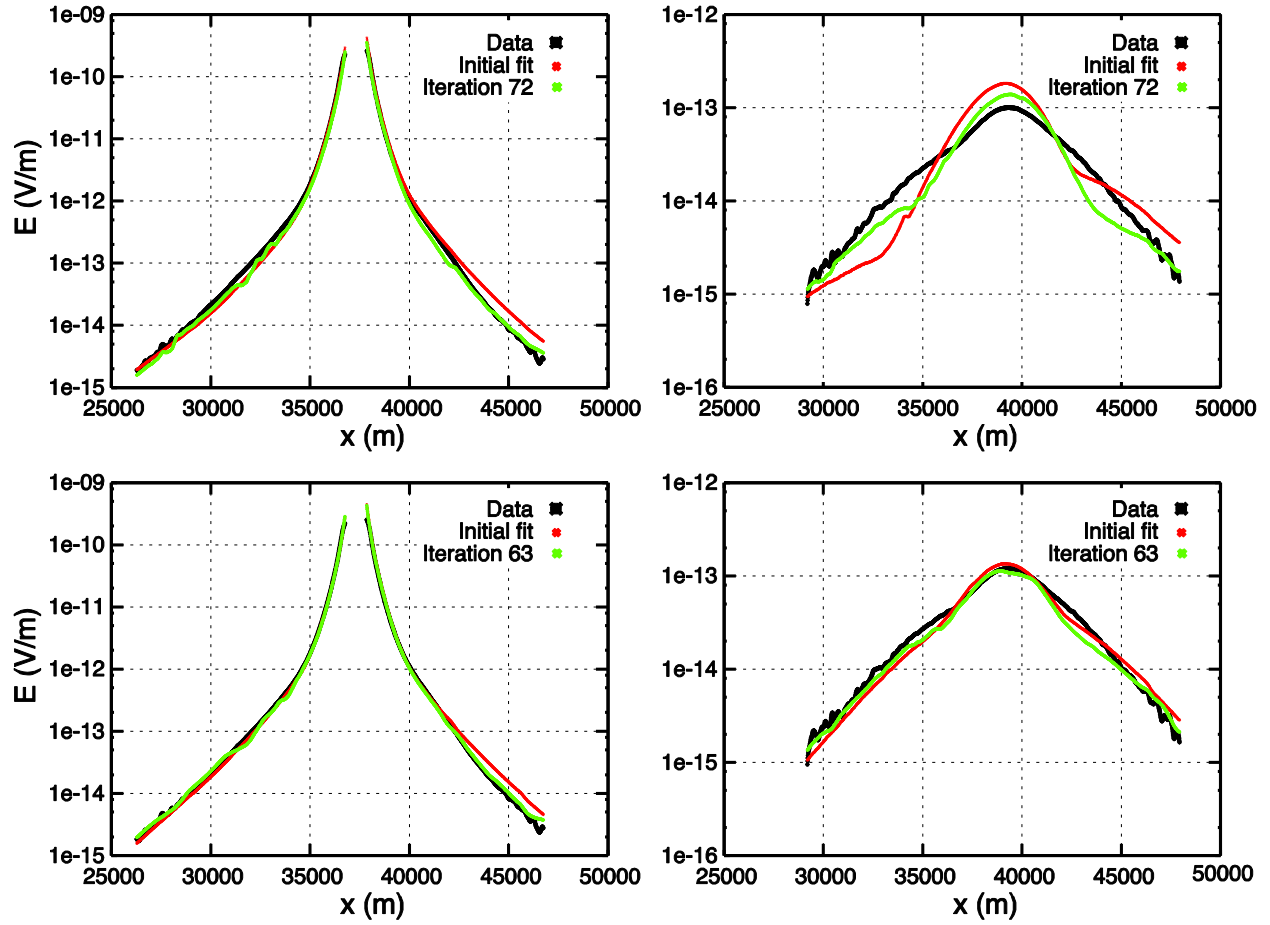


Figure 10.

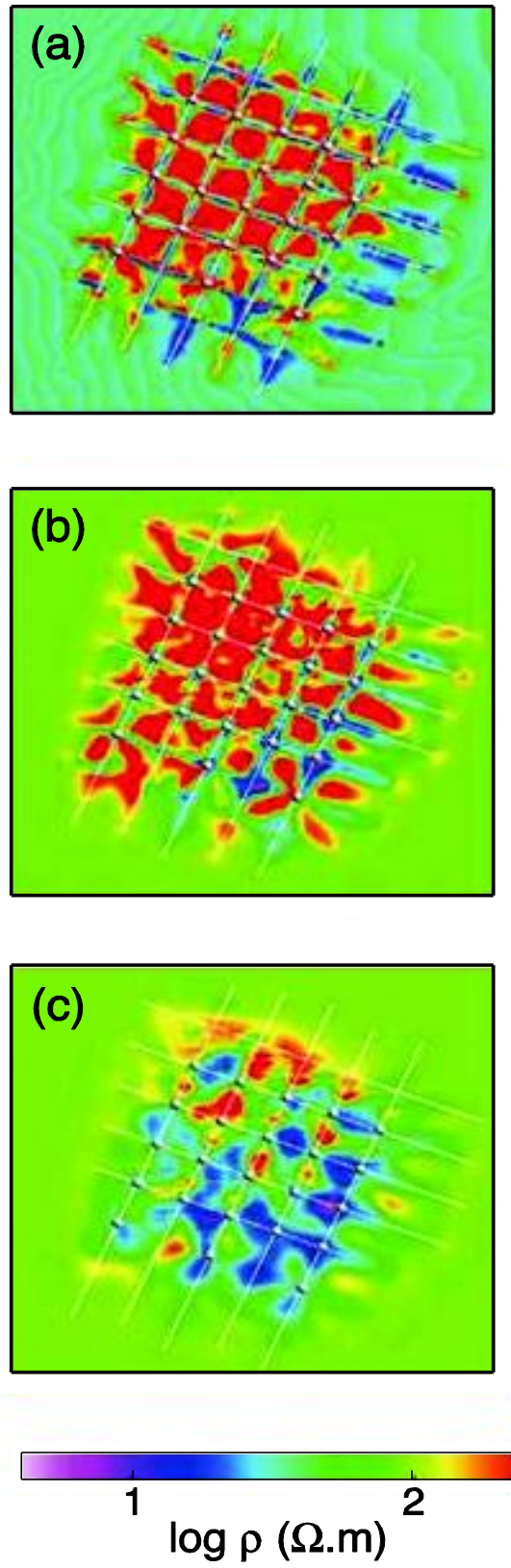


Figure 11.

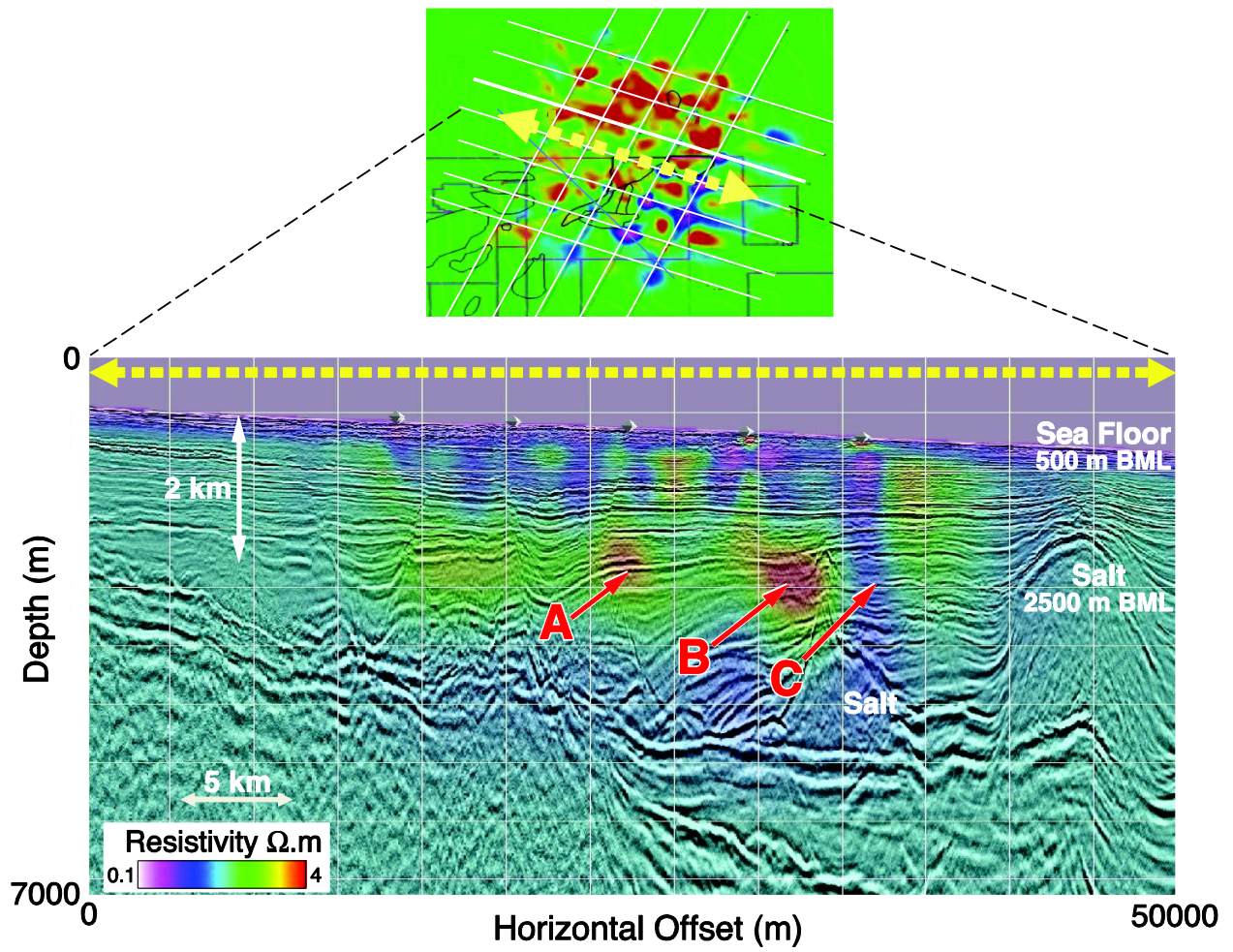


Figure 12.

$$\sigma_h = \left[\int_{x_i}^{x_{i+1}} \left(\int_{z_{k-1/2}}^{z_{k+1/2}} \sigma_h^m(x,z) dz \right)^{-1} dx \right]^{-1}$$

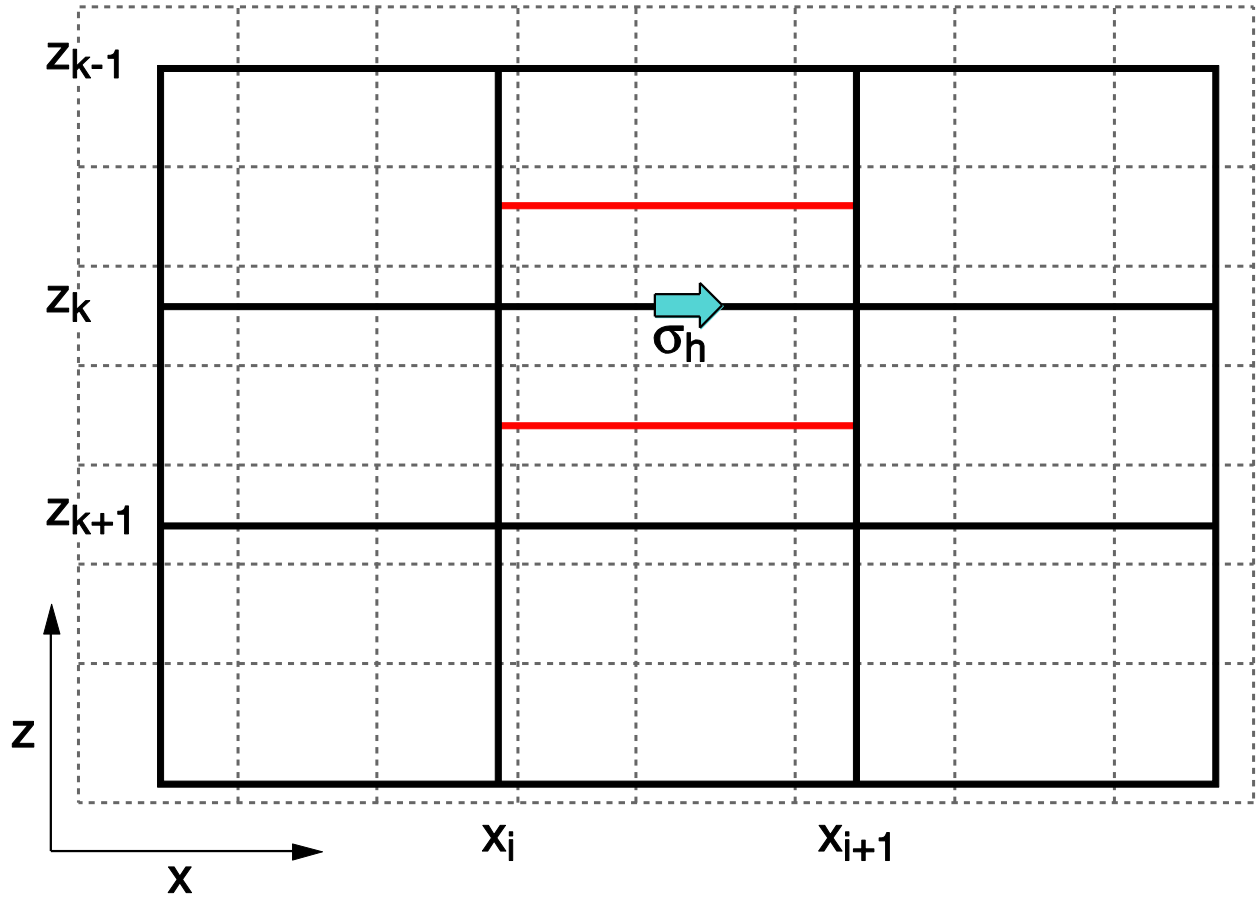


Figure 13.